nature portfolio

https://doi.org/10.1038/s41550-021-01384-2

Supplementary information

The electron-capture origin of supernova 2018zd

In the format provided by the authors and unedited

The electron-capture origin of supernova 2018zd

Daichi Hiramatsu[1,2*], D. Andrew Howell[1,2], Schuyler D. Van Dyk[3], Jared A. Goldberg[2], Keiichi Maeda[4,5], Takashi J. Moriya[6,7], Nozomu Tominaga[8,5,6], Ken'ichi Nomoto[5], Griffin Hosseinzadeh[9], Iair Arcavi[10,11], Curtis McCully[1,2], Jamison Burke[1,2], K. Azalee Bostroem[12], Stefano Valenti[12], Yize Dong[12], Peter J. Brown[13], Jennifer E. Andrews[14], Christopher Bilinski[14], G. Grant Williams[14,15], Paul S. Smith[14], Nathan Smith[14], David J. Sand[14], Gagandeep S. Anand[16,17], Chengyuan Xu[18], Alexei V. Filippenko[19,20], Melina C. Bersten[21,22,5], Gastón Folatelli[21,22,5], Patrick L. Kelly[23], Toshihide Noguchi[24], & Koichi Itagaki[25]

*Corresponding author. Email: dhiramatsu@lco.global

[1]*Las Cumbres Observatory, 6740 Cortona Drive, Suite 102, Goleta, CA 93117-5575, USA*

[2]*Department of Physics, University of California, Santa Barbara, CA 93106-9530, USA*

[3]*Caltech/Spitzer Science Center, Caltech/IPAC, Mailcode 100-22, Pasadena, CA 91125, USA*

[4]*Department of Astronomy, Kyoto University, Kitashirakawa-Oiwake-cho, Sakyo-ku, Kyoto 606-8502, Japan*

[5]*Kavli Institute for the Physics and Mathematics of the Universe (WPI), The University of Tokyo Institutes for Advanced Study, The University of Tokyo, 5-1-5 Kashiwanoha, Kashiwa, Chiba 277-8583, Japan*

[6]*National Astronomical Observatory of Japan, National Institutes of Natural Sciences, 2-21-1 Osawa, Mitaka, Tokyo 181-8588, Japan*

[7]*School of Physics and Astronomy, Faculty of Science, Monash University, Clayton, Victoria*

3800, Australia

[8]*Department of Physics, Faculty of Science and Engineering, Konan University, 8-9-1 Okamoto, Kobe, Hyogo 658-8501, Japan*

[9]*Center for Astrophysics | Harvard & Smithsonian, 60 Garden Street, Cambridge, MA 02138-1516, USA*

[10]*The School of Physics and Astronomy, Tel Aviv University, Tel Aviv 69978, Israel*

[11]*CIFAR Azrieli Global Scholars program, CIFAR, Toronto, Canada*

[12]*Department of Physics, University of California, 1 Shields Ave, Davis, CA 95616-5270, USA*

[13]*Mitchell Institute for Fundamental Physics and Astronomy, Texas A&M University, College Station, TX 77843, USA*

[14]*Steward Observatory, University of Arizona, 933 North Cherry Avenue, Tucson, AZ 85721-0065, USA*

[15]*MMT Observatory, P.O. Box 210065, Tucson, AZ 85721-0065, USA*

[16]*Infrared Processing and Analysis Center, California Institute of Technology, Pasadena, CA 91125, USA*

[17]*Institute for Astronomy, University of Hawai'i, 2680 Woodlawn Drive, Honolulu, HI 96822, USA*

[18]*Media Arts and Technology, University of California, Santa Barbara, CA 93106-6065, USA*

[19]*Department of Astronomy, University of California, Berkeley, CA 94720-3411, USA*

[20]*Miller Institute for Basic Research in Science, University of California, Berkeley, CA 94720, USA*

[21] *Instituto de Astrofísica de La Plata (IALP), CONICET, Argentina*

[22] *Facultad de Ciencias Astronómicas y Geofísicas, Universidad Nacional de La Plata, Paseo del Bosque, B1900FWA, La Plata, Argentina*

[23] *School of Physics and Astronomy, University of Minnesota, 116 Church Street SE, Minneapolis, MN 55455, USA*

[24] *Noguchi Astronomical Observatory, Katori, Chiba 287-0011, Japan*

[25] *Itagaki Astronomical Observatory, Yamagata, Yamagata 990-2492, Japan*

Supplementary Information

Follow-up imaging. Follow-up imaging was obtained with the Las Cumbres Observatory network of 0.4 m, 1 m, and 2 m telescopes[1] through the Global Supernova Project, the Neil Gehrels *Swift* Observatory Ultraviolet/Optical Telescope (UVOT), the Noguchi Astronomical Observatory (Chiba, Japan) 0.26 m telescope, and the Itagaki Astronomical Observatory (Okayama and Tochigi, Japan) 0.35 m and 0.5 m telescopes. For the Las Cumbres photometry, PSF fitting was performed using `lcogtsnpipe`[2], a PyRAF-based photometric reduction pipeline. *UBV*- and *gri*-band data were calibrated to Vega[3] and AB[4] magnitudes, respectively, using standard fields observed on the same night by the same telescope as the SN. The *Swift* UVOT photometry was conducted using the pipeline for the *Swift* Optical Ultraviolet Supernova Archive (SOUSA)[5], including the updated sensitivity corrections and zeropoints[6] and the subtraction of the underlying host-galaxy count rates using images from October/November 2019. The unfiltered optical Itagaki (KAF-1001E CCD) and Noguchi (ML0261E CCD) photometry was extracted using `Astrometrica`[7] and calibrated to the Fourth US Naval Observatory CCD Astrograph Catalog (UCAC4)[8]. All photometry will be available for download via WISeREP and the Open Supernova Catalog. We correct all photometry for the Milky Way (MW) and host-galaxy extinction (Extended Data Fig. 3).

We estimate an explosion epoch by fitting a quadratic function $F_1(t - t_0)^2$ to the unfiltered Itagaki and first three Noguchi points with similar CCD spectral responses ($\lambda_{\rm eff} = 6500$–6700 Å), where the effect of CSM interaction is less prominent than in the UV bands (Extended Data Fig. 3). This yields an explosion epoch $t_0 = {\rm MJD}\,58178.4 \pm 0.1$, where the uncertainty is estimated from the difference between the explosion epoch and the first Itagaki detection. Even if we use the most

conservative explosion epoch of the last nondetection on MJD 58175.5, the difference is only 2.9 rest-frame days, not affecting the main results of this paper.

We fit a blackbody SED to every epoch of the Las Cumbres and *Swift* photometry containing at least three filters (excluding the *r* band owing to strong Hα contamination) obtained within 0.3 d of each other to estimate the blackbody temperature and radius at the assumed luminosity distance (note that the observed SED peaks are bluer than the *Swift* wavelength coverage 3–10 d after the explosion, potentially underestimating the blackbody temperatures[2]). Then we integrate the fitted blackbody SED to obtain bolometric (and pseudobolometric) luminosity at each epoch. Since we only have the unfiltered Noguchi photometry during the plateau drop owing to the Sun constraint, we estimate a bolometric (and pseudobolometric) correction by finding the offset of the Noguchi photometry to the Las Cumbres and *Swift* integrated bolometric (and pseudobolometric) luminosity during the plateau phase (50–80 d) where most of the SED ($\sim 80\%$) is in the spectral response range of the unfiltered CCD. Then we apply the bolometric (and pseudobolometric) correction to the Noguchi photometry and include it in the bolometric (and pseudobolometric) light curve during the plateau drop (Fig. 1). This procedure is also justified by the good agreement with the tail bolometric (and pseudobolometric) luminosity obtained from the Las Cumbres multiband photometry after the Sun constraint.

Follow-up spectroscopy. Follow-up spectra were obtained with the FLOYDS spectrograph mounted on the Las Cumbres Observatory 2 m Faulkes Telescope North (FTN)[1] through the Global Supernova Project, the Boller & Chivens (B&C) spectrograph mounted on the 2.3 m Bok telescope, the Blue Channel (BC) spectrograph mounted on the 6.5 m MMT, and the Low Resolution Imag-

ing Spectrometer (LRIS)[9, 10, 11] and the DEep Imaging Multi-Object Spectrograph (DEIMOS)[12] mounted on the 10 m Keck-I and Keck-II telescopes, respectively. For the FLOYDS observations, a $2''$-wide slit was placed on the target at the parallactic angle[13] (to minimise the effects of atmospheric dispersion). One-dimensional spectra were extracted, reduced, and calibrated following standard procedures using `floyds_pipeline`[14]. The Bok low-resolution optical spectra were taken with the 300 lines mm^{-1} grating using a $1.5''$-wide slit, and the MMT moderate-resolution spectra were obtained using a $1.0''$-wide slit. The spectra were reduced using standard techniques in IRAF, including bias subtraction, flat-fielding, and sky subtraction. Flux calibration was done with spectrophotometric standard star observations taken on the same night at similar airmass. The Keck LRIS spectra were reduced using the `Lpipe` pipeline[15] with the default parameters and standard spectroscopic reduction techniques. The Keck DEIMOS spectrum was reduced with a custom-made Python pipeline that performs flat-field correction, sky subtraction, optimal extraction[16], and flux calibration using a standard star observed on the same night as the SN. All spectra will be available for download via WISeREP and the Open Supernova Catalog. We correct all spectra for the MW and host-galaxy extinction and calibrate the flux using the photometry (Extended Data Fig. 4).

We measure expansion velocities of Hα, Hβ, and Fe II λ5169 from the absorption minimum by fitting a P Cygni profile to each line in the spectra (Extended Data Fig. 4). Then we translate the difference between the observed minimum and the rest wavelength of the line to an expansion velocity using the relativistic Doppler formula (Extended Data Fig. 5). We estimate the velocity uncertainties by randomly varying the background region by ± 5 Å.

We simultaneously fit Gaussian functions to He I λ7065, [Fe II] λ7155, [Fe II] λ7172, [Ca II] λ7291, [Ca II] λ7323, [Ni II] λ7378, [Fe II] λ7388, [Ni II] λ7412, and [Fe II] λ7452 in the nebular spectra assuming a single full width at half-maximum intensity (FWHM) velocity for all lines and the theoretically expected line ratios for the [Ca II], [Fe II], and [Ni II] lines[17] (Fig. 4). The resultant [Ni II] λ7378/[Fe II] λ7155 intensity ratios and FWHM velocities are 1.3–1.6 and 2,500–2,100 km s^{-1}, respectively, from 278 to 600 d after the explosion.

Follow-up spectropolarimetry. Follow-up spectropolarimetric observations of SN 2018zd were obtained using the CCD Imaging/Spectropolarimeter (SPOL[18]) on the 6.5 m MMT telescope using a $2.8''$ slit on 2018 April 23 (53 d after the explosion). We used a 964 lines mm^{-1} grating with a typical wavelength coverage of 4,050–7,200 Å and a resolution of ~ 29 Å. We used a rotatable semi-achromatic half-wave plate to modulate incident polarization and a Wollaston prism in the collimated beam to separate the orthogonally polarized spectra onto a thinned, anti-reflection-coated 800×1200 pixel SITe CCD. The efficiency of the wave plate as a function of wavelength was measured and corrected for by inserting a fully-polarizing Nicol prism into the beam above the slit. A series of four separate exposures that sample 16 orientations of the wave plate yield two independent, background-subtracted measures of each of the linear Stokes parameters, Q and U. Two such sequences were acquired and combined to increase the signal-to-noise ratio.

Our spectropolarimetric analysis is performed primarily using the normalised linear Stokes parameters, $q = Q/I$ and $u = U/I$, which are rotated with respect to each other, allowing us to decompose the polarization signal into orthogonal components in position-angle space. We use the debiased polarization level, $p_{\rm db} = \sqrt{|(q^2 + u^2) - \frac{1}{2}(\sigma_q^2 + \sigma_u^2)|}$, in favour of the standard polar-

ization level, $p = \sqrt{q^2 + u^2}$, because the standard polarization level is a positive-definite quantity that measures the distance from the origin in a q vs. u plane. When the signal-to-noise ratio is low, this positive-definite quantity can be misleading, whereas the debiased polarization value accounts for large uncertainty in measurements of q and u.

SN 2018zd exhibits a mean polarization of 0.9% across the continuum at 5,100–5,700 Å and 0.8% across the continuum at 6,000–6,300 Å. However, the polarization does not vary much across the entire spectrum, even across absorption and emission-line features. Typically, a polarized continuum would become depolarized across emission-line features owing to dilution with unpolarized light from the emission line. Since SN 2018zd does not exhibit any such changes across any of its emission-line features, we suggest that the majority of the polarization signal arises in the interstellar medium rather than in the SN itself. The Serkowski relation[19] suggests that $p_{\max} < 9\,E(B-V)$. If all 0.9% of the continuum peak polarization in SN 2018zd were due to the interstellar medium, then we could estimate the extinction to be $E(B-V) > p_{\max}/9 = 0.1$ mag and a reddening of at least $A_V = 3.1\,E(B-V) = 0.31$ mag.

Extra `MESA+STELLA` modeling description. All progenitor models began at solar metallicity ($Z = 0.02$), and the naming scheme gives progenitor and explosion properties as follows: (M$[M_{\rm ej}/M_\odot]$_R$[R/R_\odot]$_E$[E_{\rm exp}/10^{51}\,{\rm erg}]$). The high-ejecta-mass model, M17.2_R718_E0.48, is 18.8 $M_\odot$ at core collapse (20 $M_\odot$ at zero-age main sequence (ZAMS)) with no rotation, no exponential overshooting ($f_{\rm ov} = f_{0,\rm ov} = 0.0$), mixing length $\alpha_{\rm env} = 2.0$ in the H-rich envelope, and a wind efficiency factor $\eta_{\rm wind} = 0.4$. The moderate model, M14.5_R864_E0.37, is 16.3 $M_\odot$ at core collapse (17 $M_\odot$ at ZAMS) with modest initial rotation $\Omega/\Omega_{\rm crit} = 0.2$, no ex-

ponential overshooting, $\alpha_{\rm env} = 2.0$, and $\eta_{\rm wind} = 0.2$. The low-ejecta-mass and large-radius model, M8.3_R1035_E0.23, is $11.8\,{\rm M}_\odot$ at core collapse ($15\,{\rm M}_\odot$ at ZAMS) with modest rotation $\Omega/\Omega_{\rm crit} = 0.2$, moderately high exponential overshooting ($f_{\rm ov} = 0.018, f_{\rm 0,ov} = 0.006$), $\alpha_{\rm env} = 2.0$, and $\eta_{\rm wind} = 0.9$. Despite the ZAMS mass typical of an RSG, this model sufficiently captures the relevant explosion properties for the SAGB explosion scenario, as the mass of the H-rich ejecta, explosion energy, and progenitor radius determine the plateau properties of Type II-P SNe, not the ZAMS mass.

In MESA revision 12115, a thermal bomb was injected in the innermost $0.1\,{\rm M}_\odot$ of each model, heating the star to the desired total final energy $E_{\rm exp}$, with the updated prescription for removing material falling back onto the inner boundary[20, 21], which can be relevant at the low explosion energies required here. Of the three explosions, only M8.3_R1035_E0.23 undergoes substantial late-time fallback, totaling $2\,{\rm M}_\odot$, which is excised from the model with no extra heating and negligible change in the total explosion energy. The evolution of the shock was modeled in MESA with the 'Duffell RTI' prescription for mixing via the Rayleigh-Taylor instability[22, 23], terminating near shock breakout, when the shock reaches a mass coordinate of $0.04\,{\rm M}_\odot$ below the outer boundary of each model. The ^{56}Ni distribution in each model was then scaled to match the observed value of $0.0086\,{\rm M}_\odot$. Then in STELLA, bolometric light curves and expansion velocities were produced using 600 spatial zones and 100 frequency bins, without any additional material outside the stellar photosphere. For models with CSM, 600 zones are used in STELLA, including 400 zones for the original ejecta, and 200 additional zones for the wind model.

Host galaxy. NGC 2146 is an edge-on spiral galaxy with several tidal streams that were likely ejected during a galaxy merger event $\sim 800\,\mathrm{Myr}$ ago[24] (Extended Data Fig. 1). The presence of a starburst-driven superwind from the bulge is revealed across the electromagnetic spectrum from γ-rays to infrared[25, 26, 24, 27], indicating an ongoing high star-formation rate[28] (SFR $\approx 10\,\mathrm{M}_\odot\,\mathrm{yr}^{-1}$). On the basis of radio observations of the bulge[29], there are many more dense H II regions (each containing up to 1000 type O6 stars) than supernova remnants, suggesting a relatively young phase of the starburst. The bulge has a high dust content and roughly solar metallicity ($12+\log_{10}[\mathrm{O/H}] = 8.68\pm0.10$)[28, 30]. Since SN 2018zd is at a relatively large separation from the nucleus of $1'.83$ northwest ($36''.1$ north, $103''.7$ west; Extended Data Fig. 1), and the galactic radius parameter $R_{25} = 1'.78$ (via the NASA/IPAC Extragalactic Database), if we reasonably assume that there is an abundance gradient for the galaxy, the metallicity at the SN site is likely subsolar; this merits future investigations once the SN fades.

Alternative scenarios. A low-mass ($\lesssim 9.6\,M_\odot$) Fe CCSN is a possible alternative for SN 2018zd, as similar explosion energy ($\sim 10^{50}\,\mathrm{erg}$)[31] and nucleosynthesis[32] to ECSNe may be expected because of a similar steep density gradient outside the degenerate core. For a low-mass RSG star, however, no high constant ($\gtrsim 10^{-5}\,M_\odot\,\mathrm{yr}^{-1}$)[33, 34, 35] and/or eruptive[36, 37] mass loss is expected to produce dense confined He-, C-, and N-rich, but O-poor CSM (but note that the mass loss is quite sensitive to the model treatments of, for example, convection and off-center nuclear burning[38]). In addition, a low-mass RSG has Si-, O-, and He-rich layers[39] which are expected to produce additional Si, S, Ca, Mg, O, C, and He lines in nebular spectra[40]. Thus, a low-mass Fe CCSN may be able to explain the light-curve morphology, but likely not the early-time CSM interaction and

nebular spectra observed for SN 2018zd.

On the other side of the progenitor mass spectrum, another possible alternative for SN 2018zd is a high-mass ($\gtrsim 25\,\mathrm{M}_\odot$) Fe CCSN, as small kinetic energy ($\sim 10^{50}$ erg) and ejected radioactive ^{56}Ni mass ($\lesssim 10^{-3}\,\mathrm{M}_\odot$) may be expected owing to fallback accretion onto the central remnant[41, 42]. For such high fallback accretion, however, extra luminosity ($L \propto t^{-5/3}$) at late times ($t \gtrsim 200\,\mathrm{d}$) is expected[43, 44]. Also, no ejected stable ^{58}Ni should be observed, as it is produced in the innermost neutron-rich layer[45]. Thus, a high-mass Fe CCSN may be able to explain the photospheric light curve, but not the late-time exponential tail and nebular spectra of SN 2018zd.

If the luminosity distance to NGC 2146 were larger than $12\,\mathrm{Mpc}$, it would be quite unlikely that SN 2018zd is an ECSN, since $M_{\mathrm{Ni}} > 0.01\,\mathrm{M}_\odot$, $E_{\mathrm{exp}} > 4 \times 10^{50}$ erg, and $M_{\mathrm{ej}} > 10\,\mathrm{M}_\odot$ in a reasonable progenitor radius range of 400–$1400\,\mathrm{R}_\odot$ according to the light-curve scaling (Eq. 1in Methods). Then SN 2018zd would become a real challenge to stellar evolution and SN explosion theories to reconcile all of the observational ECSN indicators with a higher M_{Ni}, E_{exp}, M_{ej}, and M_{ZAMS} for the progenitor. If the luminosity distance were $18\,\mathrm{Mpc}$, the progenitor candidate detection of SN 2018zd in *HST* F814W would become as bright as that of the SN 2005cs progenitor (Extended Data Fig. 2), but still on the faint end of Type II SN progenitors[36, 46] despite the expected higher M_{ej} and M_{ZAMS} from the light-curve scaling.

We note that Zhang et al. (2020)[47] also discusses a possible ECSN origin for SN 2018zd based on the small radioactive ^{56}Ni yield, dense CSM, and faint X-ray radiation. Owing to their adopted larger luminosity distance ($18.4 \pm 4.5\,\mathrm{Mpc}$; Methods), however, they suggest that

SN 2018zd is a member of the class of luminous Type II SNe with low expansion velocities[48], which likely arise from extended CSM interaction (4–11 weeks after the explosion). In this work, we perform numerical light-curve modeling and demonstrate that ECSN-parameter explosions with the early CSM interaction (~ 30 days after the explosion) can reproduce both the light-curve and velocity evolution (Fig. 2 and Extended Data Fig. 6). Furthermore, we present the progenitor candidate identification (Extended Data Figs. 1 and 2) and more detailed spectral analyses (Figs. 3 and 4), showing that the chemical composition and nucleosynthesis are consistent with those expected for ECSNe.

Other ECSN candidates. SN 1054, whose remnant is the Crab Nebula, has been suggested as an ECSN candidate[49, 50, 51, 52, 53, 54]. It shows He-, C-, and Ni-rich ejecta, but O- and Fe-poor abundances[55, 56], small ejecta mass ($4.6 \pm 1.8\,\mathrm{M}_\odot$)[57], and low kinetic energy ($\sim 10^{49}$ erg)[52]. The slowly expanding filaments ($\sim 1200\,\mathrm{km\,s^{-1}}$) without a blast wave outside likely indicate the presence of CSM decelerating the SN ejecta[57, 52], and the historical light curve of SN 1054 may be similar to that of ECSNe[52, 53, 54]. However, the observed relatively high neutron star kick velocity ($\sim 160\,\mathrm{km\,s^{-1}}$) is at odds with those theoretically predicted for ECSNe ($< 10\,\mathrm{km\,s^{-1}}$)[58]. On the other hand, the pre-collapse O+Ne+Mg core of an SAGB star could have large rotation and even 'super-Chandrasekhar' mass if the angular momentum transport from the rotating core to the very extended SAGB envelope is small during contraction[59, 60, 61]. The collapse of such an unstable core could in principle yield a large spin and kick.

In addition to SN 1054, other previously suggested ECSN candidates can be divided into three main types: intermediate-luminosity red transients[62, 63, 64, 65, 66, 67] (ILRTs; for example, SN 2008S

and AT 2017be), low-luminosity Type II-P SNe[68, 69, 70, 71], and Type IIn-P SNe (for example, SNe 2009kn and 2011ht)[72, 73, 54, 52] (Extended Data Fig. 7).

ILRTs are the luminosity gap transients between novae and SNe, whose origin has been debated as either a massive-star outburst[74, 75, 76, 77] or a terminal ECSN explosion[62, 63, 64, 65, 66, 67]. Their progenitors are surrounded by dusty, optically thick shells, resulting in CSM-dominated transients[62, 63, 64, 74, 75, 65]. However, their faint light-curve morphology with CSM interaction requires extremely low explosion energy ($\lesssim 10^{48}$ erg) that is unexpected for ECSNe[53, 54, 78], and their chemical composition and nucleosynthesis are unclear owing to the lack of nebular-phase spectra.

Low-luminosity Type II-P SNe typically yield low ^{56}Ni mass ($\lesssim 10^{-2}\,\mathrm{M}_{\odot}$)[70] with ECSN-like light-curve morphology (Fig. 1). However, their chemical composition and nucleosynthesis are inconsistent with ECSNe[40] (Supplementary Fig. 2), and their CSM density is generally low compared to that expected from ECSNe[79, 54] (except for SN 2016bkv[71]). Low-mass RSG progenitors have been directly identified for SNe 2003gd[80], 2005cs[81, 80], and 2008bk[82], excluding SAGB stars – the progenitors of ECSNe.

Type IIn-P SNe show Type IIn-like narrow CSM emission lines in spectra and Type II-P-like light-curve morphology with large plateau drops similar to ECSNe[72, 73, 52, 54] (Supplementary Fig. 1). The SN signatures (for example, chemical abundance) are mostly hidden below the CSM interaction, in general. For Type IIn-P SN 2011ht[83], however, we measure [Ni II] λ7378/[Fe II] $\lambda7155 = 3.8$ at $155\,\mathrm{d}$ after the explosion (using a public spectrum on WISeREP), which may

indicate ECSN-like nucleosynthesis, although the spectrum may not be fully nebular given the relatively early phase. While no SN IIn-P progenitors have been directly identified, a pre-explosion outburst has been observed for SN 2011ht[84]. The true nature of Type IIn-P SNe is yet to be revealed.

Supplementary References

1. Brown, T. M. *et al.* Las Cumbres Observatory Global Telescope Network. *Publ. Astron. Soc. Pac.* **125**, 1031 (2013).

2. Valenti, S. *et al.* The diversity of Type II supernova versus the similarity in their progenitors. *Mon. Not. R. Astron. Soc.* **459**, 3939–3962 (2016).

3. Stetson, P. B. Homogeneous Photometry for Star Clusters and Resolved Galaxies. II. Photometric Standard Stars. *Publ. Astron. Soc. Pac.* **112**, 925–931 (2000).

4. Albareti, F. D. *et al.* The 13th Data Release of the Sloan Digital Sky Survey: First Spectroscopic Data from the SDSS-IV Survey Mapping Nearby Galaxies at Apache Point Observatory. *Astrophys. J. Suppl.* **233**, 25 (2017).

5. Brown, P. J., Breeveld, A. A., Holland, S., Kuin, P. & Pritchard, T. SOUSA: the Swift Optical/Ultraviolet Supernova Archive. *Astrophys. Space Sci.* **354**, 89–96 (2014).

6. Breeveld, A. A. *et al.* An Updated Ultraviolet Calibration for the Swift/UVOT. In McEnery, J. E., Racusin, J. L. & Gehrels, N. (eds.) *American Institute of Physics Conference Series*, vol. 1358 of *American Institute of Physics Conference Series*, 373–376 (2011).

7. Raab, H. Astrometrica: Astrometric data reduction of CCD images (2012).

8. Zacharias, N. *et al.* The Fourth US Naval Observatory CCD Astrograph Catalog (UCAC4). *Astron. J.* **145**, 44 (2013).

9. Oke, J. B. *et al.* The Keck Low-Resolution Imaging Spectrometer. *Publ. Astron. Soc. Pac.* **107**, 375 (1995).

10. McCarthy, J. K. *et al. Blue channel of the Keck low-resolution imaging spectrometer*, vol. 3355 of *Society of Photo-Optical Instrumentation Engineers (SPIE) Conference Series*, 81–92 (Optical Astronomical Instrumentation, 1998).

11. Rockosi, C. *et al. The low-resolution imaging spectrograph red channel CCD upgrade: fully depleted, high-resistivity CCDs for Keck*, vol. 7735 of *Society of Photo-Optical Instrumentation Engineers (SPIE) Conference Series*, 77350R (Optical Astronomical Instrumentation, 2010).

12. Faber, S. M. *et al. The DEIMOS spectrograph for the Keck II Telescope: integration and testing*, vol. 4841 of *Society of Photo-Optical Instrumentation Engineers (SPIE) Conference Series*, 1657–1669 (2003).

13. Filippenko, A. V. The importance of atmospheric differential refraction in spectrophotometry. *Publ. Astron. Soc. Pac.* **94**, 715–721 (1982).

14. Valenti, S. *et al.* The first month of evolution of the slow-rising Type IIP SN 2013ej in M74. *Mon. Not. R. Astron. Soc.* **438**, L101–L105 (2014).

15. Perley, D. A. Fully Automated Reduction of Longslit Spectroscopy with the Low Resolution Imaging Spectrometer at the Keck Observatory. *Publ. Astron. Soc. Pac.* **131**, 084503 (2019).

16. Horne, K. An optimal extraction algorithm for CCD spectroscopy. *Publ. Astron. Soc. Pac.* **98**, 609–617 (1986).

17. Jerkstrand, A. *et al.* Supersolar Ni/Fe production in the Type IIP SN 2012ec. *Mon. Not. R. Astron. Soc.* **448**, 2482–2494 (2015).

18. Schmidt, G. D., Stockman, H. S. & Smith, P. S. Discovery of a Sub-Megagauss Magnetic White Dwarf through Spectropolarimetry. *Astrophys. J. Lett.* **398**, L57 (1992).

19. Serkowski, K., Mathewson, D. S. & Ford, V. L. Wavelength dependence of interstellar polarization and ratio of total to selective extinction. *Astrophys. J.* **196**, 261–290 (1975).

20. Paxton, B. *et al.* Modules for Experiments in Stellar Astrophysics (MESA): Pulsating Variable Stars, Rotation, Convective Boundaries, and Energy Conservation. *Astrophys. J. Suppl.* **243**, 10 (2019).

21. Goldberg, J. A., Bildsten, L. & Paxton, B. Inferring Explosion Properties from Type II-Plateau Supernova Light Curves. *Astrophys. J.* **879**, 3 (2019).

22. Duffell, P. C. A One-Dimensional Model for Rayleigh-Taylor Instability in Supernova Remnants. *Astrophys. J.* **821**, 76 (2016).

23. Paxton, B. *et al.* Modules for Experiments in Stellar Astrophysics (MESA): Convective Boundaries, Element Diffusion, and Massive Star Explosions. *Astrophys. J. Suppl.* **234**, 34 (2018).

24. Taramopoulos, A., Payne, H. & Briggs, F. H. HI observations of the starburst galaxy NGC 2146. *Astron. Astrophys.* **365**, 360–369 (2001).

25. Tang, Q.-W., Wang, X.-Y. & Tam, P.-H. T. Discovery of GeV Emission from the Direction of the Luminous Infrared Galaxy NGC 2146. *Astrophys. J.* **794**, 26 (2014).

26. Armus, L., Heckman, T. M., Weaver, K. A. & Lehnert, M. D. ROSAT Observations of NGC 2146: Evidence for a Starburst-driven Superwind. *Astrophys. J.* **445**, 666 (1995).

27. Kreckel, K. *et al.* A Far-IR View of the Starburst-driven Superwind in NGC 2146. *Astrophys. J.* **790**, 26 (2014).

28. Skibba, R. A. *et al.* The Emission by Dust and Stars of Nearby Galaxies in the Herschel KINGFISH Survey. *Astrophys. J.* **738**, 89 (2011).

29. Tarchi, A. *et al.* Radio supernovae, supernova remnants and H II regions in NGC 2146 observed with MERLIN and the VLA. *Astron. Astrophys.* **358**, 95–103 (2000).

30. Aniano, G. *et al.* Modeling Dust and Starlight in Galaxies Observed by Spitzer and Herschel: The KINGFISH Sample. *Astrophys. J.* **889**, 150 (2020).

31. Müller, B. *et al.* Three-dimensional simulations of neutrino-driven core-collapse supernovae from low-mass single and binary star progenitors. *Mon. Not. R. Astron. Soc.* **484**, 3307–3324 (2019).

32. Wanajo, S., Müller, B., Janka, H.-T. & Heger, A. Nucleosynthesis in the Innermost Ejecta of Neutrino-driven Supernova Explosions in Two Dimensions. *Astrophys. J.* **852**, 40 (2018).

33. Mauron, N. & Josselin, E. The mass-loss rates of red supergiants and the de Jager prescription. *Astron. Astrophys.* **526**, A156 (2011).

34. Goldman, S. R. *et al.* The wind speeds, dust content, and mass-loss rates of evolved AGB and RSG stars at varying metallicity. *Mon. Not. R. Astron. Soc.* **465**, 403–433 (2017).

35. Beasor, E. R. *et al.* A new mass-loss rate prescription for red supergiants. *Mon. Not. R. Astron. Soc.* **492**, 5994–6006 (2020).

36. Smartt, S. J. Progenitors of Core-Collapse Supernovae. *Ann. Rev. Astron. Astrophys.* **47**, 63–106 (2009).

37. Fuller, J. Pre-supernova outbursts via wave heating in massive stars - I. Red supergiants. *Mon. Not. R. Astron. Soc.* **470**, 1642–1656 (2017).

38. Woosley, S. E. & Heger, A. The Remarkable Deaths of 9-11 Solar Mass Stars. *Astrophys. J.* **810**, 34 (2015).

39. Jones, S. *et al.* Advanced Burning Stages and Fate of 8-10 $M_\odot$ Stars. *Astrophys. J.* **772**, 150 (2013).

40. Jerkstrand, A. *et al.* Emission line models for the lowest mass core-collapse supernovae - I. Case study of a 9 $M_{\odot}$ one-dimensional neutrino-driven explosion. *Mon. Not. R. Astron. Soc.* **475**, 277–305 (2018).

41. Lisakov, S. M., Dessart, L., Hillier, D. J., Waldman, R. & Livne, E. Progenitors of low-luminosity Type II-Plateau supernovae. *Mon. Not. R. Astron. Soc.* **473**, 3863–3881 (2018).

42. Chan, C., Müller, B., Heger, A., Pakmor, R. & Springel, V. Black Hole Formation and Fallback during the Supernova Explosion of a 40 $M_{\odot}$ Star. *Astrophys. J. Lett.* **852**, L19 (2018).

43. Dexter, J. & Kasen, D. Supernova Light Curves Powered by Fallback Accretion. *Astrophys. J.* **772**, 30 (2013).

44. Moriya, T. J., Müller, B., Chan, C., Heger, A. & Blinnikov, S. I. Fallback Accretion-powered Supernova Light Curves Based on a Neutrino-driven Explosion Simulation of a 40 $M_{\odot}$ Star. *Astrophys. J.* **880**, 21 (2019).

45. Wanajo, S., Nomoto, K., Janka, H. T., Kitaura, F. S. & Müller, B. Nucleosynthesis in Electron Capture Supernovae of Asymptotic Giant Branch Stars. *Astrophys. J.* **695**, 208–220 (2009).

46. Smartt, S. J. Observational Constraints on the Progenitors of Core-Collapse Supernovae: The Case for Missing High-Mass Stars. *Publ. Astron. Soc. Aust.* **32**, e016 (2015).

47. Zhang, J. *et al.* SN 2018zd: an unusual stellar explosion as part of the diverse Type II Supernova landscape. *Mon. Not. R. Astron. Soc.* **498**, 84–100 (2020).

48. Rodríguez, Ó. *et al.* Luminous Type II supernovae for their low expansion velocities. *Mon. Not. R. Astron. Soc.* **494**, 5882–5901 (2020).

49. Nomoto, K. *et al.* The Crab Nebula's progenitor. *Nature* **299**, 803–805 (1982).

50. Nomoto, K. Evolution of 8-10 solar mass stars toward electron capture supernovae. I - Formation of electron-degenerate O + NE + MG cores. *Astrophys. J.* **277**, 791–805 (1984).

51. Nomoto, K. Evolution of 8–10 $M_{\odot}$ Stars toward Electron Capture Supernovae. II. Collapse of an O + NE + MG Core. *Astrophys. J.* **322**, 206 (1987).

52. Smith, N. The Crab nebula and the class of Type IIn-P supernovae caused by sub-energetic electron-capture explosions. *Mon. Not. R. Astron. Soc.* **434**, 102–113 (2013).

53. Tominaga, N., Blinnikov, S. I. & Nomoto, K. Supernova Explosions of Super-asymptotic Giant Branch Stars: Multicolor Light Curves of Electron-capture Supernovae. *Astrophys. J. Lett.* **771**, L12 (2013).

54. Moriya, T. J. *et al.* Electron-capture supernovae exploding within their progenitor wind. *Astron. Astrophys.* **569**, A57 (2014).

55. Hudgins, D., Herter, T. & Joyce, R. J. The Ni/Fe Ratio in the Crab Nebula. *Astrophys. J. Lett.* **354**, L57 (1990).

56. Satterfield, T. J., Katz, A. M., Sibley, A. R., MacAlpine, G. M. & Uomoto, A. Element Distributions in the Crab Nebula. *Astron. J.* **144**, 27 (2012).

57. Fesen, R. A., Shull, J. M. & Hurford, A. P. An Optical Study of the Circumstellar Environment Around the Crab Nebula. *Astron. J.* **113**, 354–363 (1997).

58. Gessner, A. & Janka, H.-T. Hydrodynamical Neutron-star Kicks in Electron-capture Supernovae and Implications for the CRAB Supernova. *Astrophys. J.* **865**, 61 (2018).

59. Uenishi, T., Nomoto, K. & Hachisu, I. Evolution of Rotating Accreting White Dwarfs and the Diversity of Type Ia Supernovae. *Astrophys. J.* **595**, 1094–1100 (2003).

60. Benvenuto, O. G., Panei, J. A., Nomoto, K., Kitamura, H. & Hachisu, I. Final Evolution and Delayed Explosions of Spinning White Dwarfs in Single Degenerate Models for Type Ia Supernovae. *Astrophys. J. Lett.* **809**, L6 (2015).

61. Hachisu, I., Kato, M., Saio, H. & Nomoto, K. A Single Degenerate Progenitor Model for Type Ia Supernovae Highly Exceeding the Chandrasekhar Mass Limit. *Astrophys. J.* **744**, 69 (2012).

62. Prieto, J. L. *et al.* Discovery of the Dust-Enshrouded Progenitor of SN 2008S with Spitzer. *Astrophys. J. Lett.* **681**, L9 (2008).

63. Botticella, M. T. *et al.* SN 2008S: an electron-capture SN from a super-AGB progenitor? *Mon. Not. R. Astron. Soc.* **398**, 1041–1068 (2009).

64. Thompson, T. A. *et al.* A New Class of Luminous Transients and a First Census of their Massive Stellar Progenitors. *Astrophys. J.* **705**, 1364–1384 (2009).

65. Adams, S. M. *et al.* Almost gone: SN 2008S and NGC 300 2008OT-1 are fainter than their progenitors. *Mon. Not. R. Astron. Soc.* **460**, 1645–1657 (2016).

66. Cai, Y. Z. *et al.* AT 2017be - a new member of the class of intermediate-luminosity red transients. *Mon. Not. R. Astron. Soc.* **480**, 3424–3445 (2018).

67. Stritzinger, M. D. *et al.* The Carnegie Supernova Project II. Observations of the intermediate-luminosity red transient SNhunt120. *Astron. Astrophys.* **639**, A103 (2020).

68. Kitaura, F. S., Janka, H. T. & Hillebrandt, W. Explosions of O-Ne-Mg cores, the Crab supernova, and subluminous type II-P supernovae. *Astron. Astrophys.* **450**, 345–350 (2006).

69. Janka, H. T., Müller, B., Kitaura, F. S. & Buras, R. Dynamics of shock propagation and nucleosynthesis conditions in O-Ne-Mg core supernovae. *Astron. Astrophys.* **485**, 199–208 (2008).

70. Spiro, S. *et al.* Low luminosity Type II supernovae - II. Pointing towards moderate mass precursors. *Mon. Not. R. Astron. Soc.* **439**, 2873–2892 (2014).

71. Hosseinzadeh, G. *et al.* Short-lived Circumstellar Interaction in the Low-luminosity Type IIP SN 2016bkv. *Astrophys. J.* **861**, 63 (2018).

72. Kankare, E. *et al.* SN 2009kn - the twin of the Type IIn supernova 1994W. *Mon. Not. R. Astron. Soc.* **424**, 855–873 (2012).

73. Mauerhan, J. C. *et al.* SN 2011ht: confirming a class of interacting supernovae with plateau light curves (Type IIn-P). *Mon. Not. R. Astron. Soc.* **431**, 2599–2611 (2013).

74. Bond, H. E. *et al.* The 2008 Luminous Optical Transient in the Nearby Galaxy NGC 300. *Astrophys. J. Lett.* **695**, L154–L158 (2009).

75. Berger, E. *et al.* An Intermediate Luminosity Transient in NGC 300: The Eruption of a Dust-Enshrouded Massive Star. *Astrophys. J.* **699**, 1850–1865 (2009).

76. Smith, N. *et al.* SN 2008S: A Cool Super-Eddington Wind in a Supernova Impostor. *Astrophys. J. Lett.* **697**, L49–L53 (2009).

77. Smith, N., Li, W., Silverman, J. M., Ganeshalingam, M. & Filippenko, A. V. Luminous blue variable eruptions and related transients: diversity of progenitors and outburst properties. *Mon. Not. R. Astron. Soc.* **415**, 773–810 (2011).

78. Moriya, T. J. & Eldridge, J. J. Rapidly evolving faint transients from stripped-envelope electron-capture supernovae. *Mon. Not. R. Astron. Soc.* **461**, 2155–2161 (2016).

79. Poelarends, A. J. T., Herwig, F., Langer, N. & Heger, A. The Supernova Channel of Super-AGB Stars. *Astrophys. J.* **675**, 614–625 (2008).

80. Maund, J. R., Reilly, E. & Mattila, S. A late-time view of the progenitors of five Type IIP supernovae. *Mon. Not. R. Astron. Soc.* **438**, 938–958 (2014).

81. Eldridge, J. J., Mattila, S. & Smartt, S. J. Ruling out a massive asymptotic giant-branch star as the progenitor of supernova 2005cs. *Mon. Not. R. Astron. Soc.* **376**, L52–L56 (2007).

82. Maund, J. R., Mattila, S., Ramirez-Ruiz, E. & Eldridge, J. J. A new precise mass for the progenitor of the Type IIP SN 2008bk. *Mon. Not. R. Astron. Soc.* **438**, 1577–1592 (2014).

83. Humphreys, R. M. *et al.* The Unusual Temporal and Spectral Evolution of SN2011ht. II. Peculiar Type IIn or Impostor? *Astrophys. J.* **760**, 93 (2012).

84. Fraser, M. *et al.* Detection of an Outburst One Year Prior to the Explosion of SN 2011ht. *Astrophys. J. Lett.* **779**, L8 (2013).

85. Smith, N., Li, W., Filippenko, A. V. & Chornock, R. Observed fractions of core-collapse supernova types and initial masses of their single and binary progenitor stars. *Mon. Not. R. Astron. Soc.* **412**, 1522–1538 (2011).

86. Taddia, F. *et al.* Carnegie Supernova Project: Observations of Type IIn supernovae. *Astron. Astrophys.* **555**, A10 (2013).

87. de Jaeger, T. *et al.* SN 2011A: A Low-luminosity Interacting Transient with a Double Plateau and Strong Sodium Absorption. *Astrophys. J.* **807**, 63 (2015).

88. Hamuy, M. Observed and Physical Properties of Core-Collapse Supernovae. *Astrophys. J.* **582**, 905–914 (2003).

89. Benetti, S. *et al.* The fading of supernova 1997D. *Mon. Not. R. Astron. Soc.* **322**, 361–368 (2001).

90. Pastorello, A. *et al.* SN 2005cs in M51 - II. Complete evolution in the optical and the near-infrared. *Mon. Not. R. Astron. Soc.* **394**, 2266–2282 (2009).

91. Van Dyk, S. D. *et al.* Supernova 2008bk and Its Red Supergiant Progenitor. *Astron. J.* **143**, 19 (2012).

92. Maguire, K. *et al.* Constraining the physical properties of Type II-Plateau supernovae using nebular phase spectra. *Mon. Not. R. Astron. Soc.* **420**, 3451–3468 (2012).

93. Gutiérrez, C. P. *et al.* Type II Supernova Spectral Diversity. I. Observations, Sample Characterization, and Spectral Line Evolution. *Astrophys. J.* **850**, 89 (2017).

Supplementary Figures

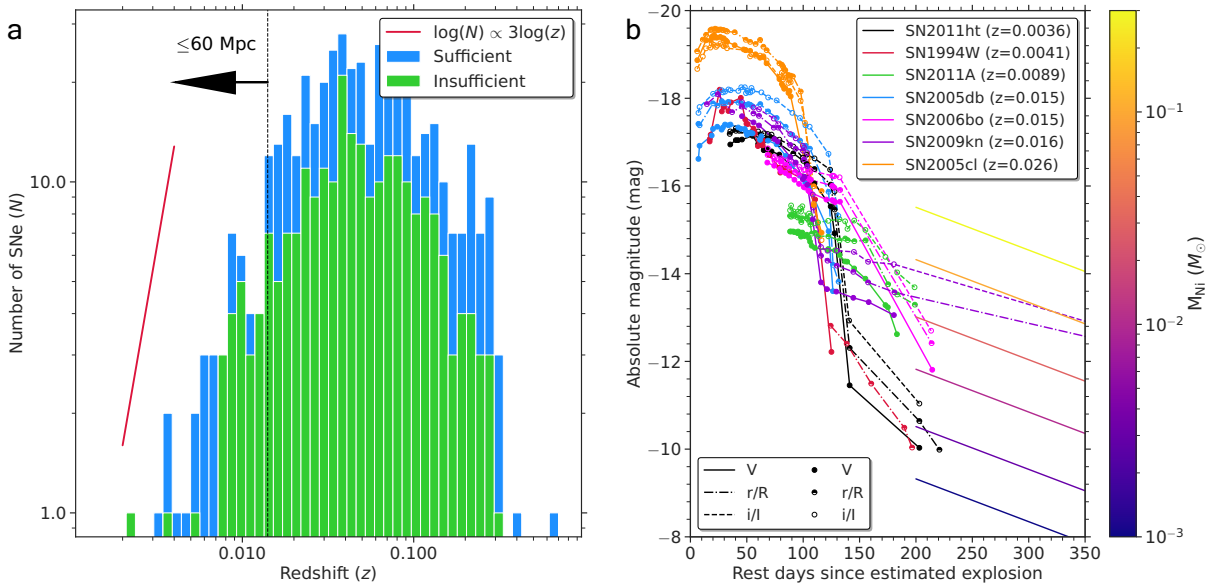

Supplementary Figure 1 **Public Type IIn and IIn-P SN samples.** **a,** Redshift distribution of the 455 public Type IIn SNe retrieved from WISeREP and/or TNS. 241 objects have insufficient public spectra and/or light curves to secure the Type IIn classifications and/or to be identified as Type IIn-P SNe, but are included in the sample so as not to overestimate the lower limit. The red line is the number-density slope by assuming the volume term with the standard cosmology ($H_0 = 71.0$ km s^{-1} Mpc^{-1}, $\Omega_{\Lambda_0} = 0.7$, and $\Omega_{m_0} = 0.3$, giving $d_L \propto z$ for $z < 0.1$). The black dotted line is the distance cut (≤ 60 Mpc) we apply to compare with the LOSS sample[85]. By comparing the number-density slope to the sample histogram as a first-order estimation, the sample does not seem to suffer substantially from incompleteness within 60 Mpc. **b,** Comparison of the identified Type IIn-P SN candidates by applying the two light-curve criteria. The explosion epochs of SNe 2006bo and 2011A are not well constrained and can shift up to ± 64 d and ± 85 d, respectively[86, 87].

The colour-coded tails at 200–350 d are the expected V-band tails from the fully trapped radioactive heating for a given ^{56}Ni mass[88]. The observed Ni-mass upper limits are within 10^{-3} to $3 \times 10^{-2}\,\mathrm{M}_{\odot}$, assuming that the tails are purely powered by the radioactive heating.

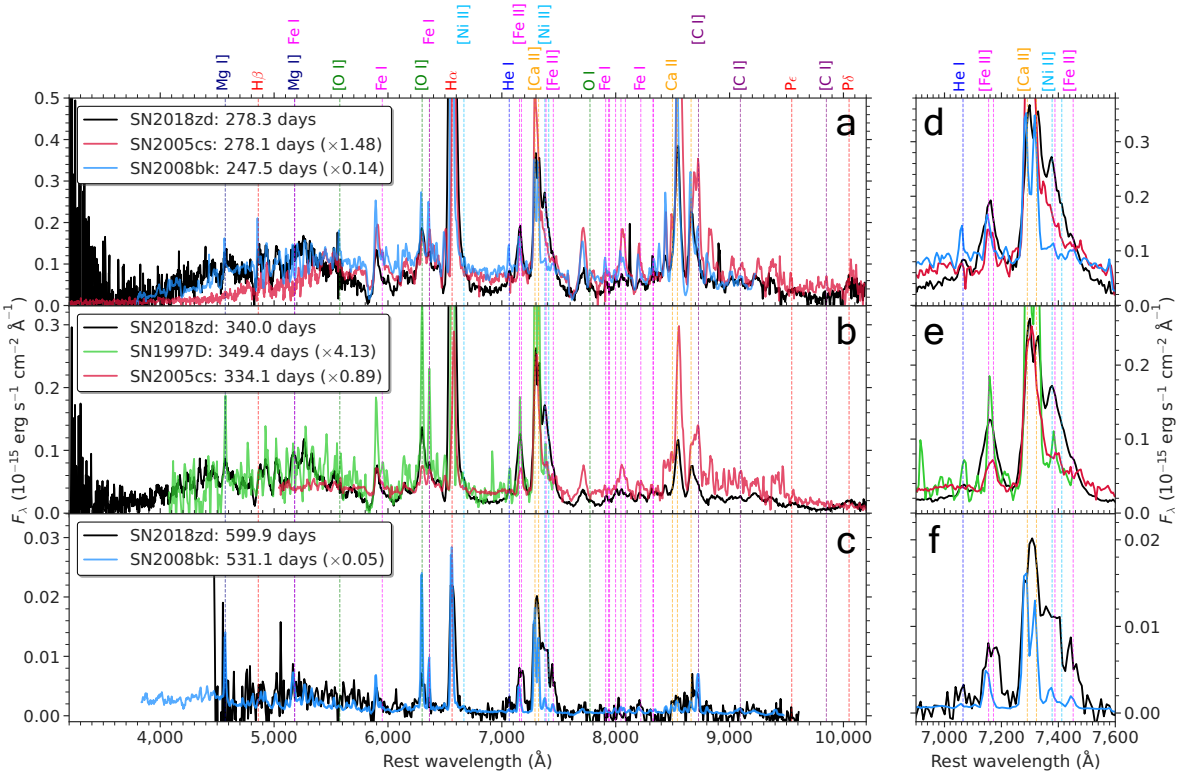

Supplementary Figure 2 Nebular spectral time series of low-luminosity Type II-P SNe. a–c, Comparison of the nebular spectral time series at three different epochs of SN 2018zd with the scaled (by integrated flux as in the legend) and resampled low-luminosity Type II-P SNe 1997D[89], 2005cs[90], and 2008bk[91, 92, 93]. In ascending order of wavelength, note the distinct Mg I] λ4571 and [O I] $\lambda\lambda$6300, 6364 + Fe I λ6364 observed in SN 1997D; Fe I cluster 7,900–8,500 Å, [C I] λ8727, and [C I] λ9100 observed in SN 2005cs; and Mg I] λ4571, [O I] $\lambda\lambda$6300, 6364 + Fe I λ6364, Fe I cluster 7,900–8,500 Å, and [C I] λ8727 observed in SN 2008bk. **d–f,** Same as panels (**a, b, c**), but zoomed into the wavelength range of interest (as in Fig. 4). Note the line-intensity ratios of [Ni II] λ7378/[Fe II] λ7155 < 1 observed in SNe 1997D, 2005cs, and 2008bk. The strong C, O,

Mg, and/or Fe lines combined with the weak Ni lines observed in SNe 1997D, 2005cs, and 2008bk are inconsistent with the ECSN chemical composition and nucleosynthesis.